Chinese Chemical Letters 37 (2026) 112234

Contents lists available at ScienceDirect

Chinese Chemical Letters

journal homepage: www.elsevier.com/locate/cclet

Construction of tri-input DNA circuits *via* a double-blocking strategy for spatiotemporally precise *in vivo* fluorescence imaging

Liuyan Zhou[1], Luyin Wang[1], Xiaolu Li, Meiling Ren, Shengqiang Hu*, Mengjiao Huang, Shulin Zhao, Liangliang Zhang*

Key Laboratory for Chemistry and Molecular Engineering of Medicinal Resources (Ministry of Education of China), Guangxi Key Laboratory of Chemistry and Molecular Engineering of Medicinal Resources, University Engineering Research Center for Chemistry of Characteristic Medicinal Resources (Guangxi), School of Chemistry and Pharmaceutical Sciences, Guangxi Normal University, Guilin 541004, China

ARTICLE INFO

Article history:
Received 14 September 2025
Revised 29 November 2025
Accepted 8 December 2025
Available online 10 December 2025

Keywords:
Tri-input DNA circuits
DNAzyme-based walking system
Upconversion nanoparticles
Spatiotemporal control
Fluorescence imaging

ABSTRACT

Owing to their sophisticated information-processing capabilities, multi-input DNA circuits (DCs) show great potential in spatiotemporally precise *in vivo* imaging of diseases. Nevertheless, engineering simple yet versatile multi-input DCs remain a big challenge. Herein, tri-input DNA circuits (tiDCs) based on a DNAzyme-driven walker system were developed *via* a novel double-blocking strategy, enabling high spatiotemporal-precision fluorescence imaging *in vivo*. A hairpin structure containing photocleavable linker was designed as the first blocking unit to lock the miRNA-complementary strand, while the miRNA-complementary strand was introduced as the second blocking unit to inhibit the Zn^{2+}-specific DNAzyme-contained walker strand. By leveraging upconversion nanoparticles for targeted delivery and light transduction, the tiDCs generated amplified fluorescence signals exclusively upon simultaneous inputs of near-infrared (NIR) light, miRNA, and Zn^{2+}, achieving spatiotemporally controlled imaging of arthritis. This work establishes a programmable molecular platform for visualizing complex biological systems *in vivo*, offering new pathways to advance diagnostic precision and therapeutic outcomes.

© 2026 Published by Elsevier B.V. on behalf of Chinese Chemical Society and Institute of Materia Medica, Chinese Academy of Medical Sciences.

The occurrence and progression of diseases involve a complex interplay of multiple biomarkers, such as miRNA and metal ions [1,2]. In contrast to single-biomarker designs, fluorescent probes that incorporate multiple biomarkers as activators can significantly improve diagnostic reliability and accuracy [3,4]. In view of this importance, numerous novel fluorescent probes have been developed, including peptide probes [5], DNA probes [6], and quantum dots nanoprobes [7]. Despite significant advancements, achieving precise spatiotemporal control, particularly at desired times and locations, remains a challenge for most multiple biomarkers-activated probes [8,9]. A key limitation lies in the fact that introducing external control mechanisms often disrupts their inherent multi-biomarker activation capability. In response, light has been incorporated as an external stimulus in the design of fluorescent probes. Among available options, near-infrared (NIR) light induces minimal photodamage and enables deeper tissue penetration compared to ultraviolet (UV) or blue light, thereby offering superior spatiotemporal control in biological systems [10,11]. Recently, lanthanide-doped upconversion nanoparticles (UCNPs), which absorb NIR light and emit UV-vis radiation, have been developed as NIR-to-UV transducers to enable light-gated fluorescence imaging [12,13]. Furthermore, owing to their enhanced permeability and retention (EPR) effect [14,15], UCNPs can passively accumulate in tumors. Consequently, integrating UCNPs into multiple biomarkers-activated nanoprobes through modular assembly of functional units promises significantly enhanced precision for *in vivo* imaging with high spatiotemporal resolution [16,17]. Nevertheless, the construction of a single probe capable of reliable multi-input activation by orthogonally combining UCNP-mediated NIR light with several biomarkers remains a critical and unresolved design challenge.

Owing to its precise base-pairing property, DNA has emerged as a programmable molecular building block for constructing various nanostructures capable of executing computational tasks in response to specific molecular inputs [18,19]. DNA circuits (DCs), in particular, have garnered significant attention due to their capacity for multiplexed parallel recognition of biomarkers (*e.g.*, nucleic acids, metal ions, or enzymes) and subsequent execution of Boolean logic operations [20]. These DCs generate a single

* Corresponding authors.
E-mail addresses: zn_sqhu@163.com (S. Hu), liangzhang319@163.com (L. Zhang).
[1] These authors contributed equally to this work.

https://doi.org/10.1016/j.cclet.2025.112234
1001-8417/© 2026 Published by Elsevier B.V. on behalf of Chinese Chemical Society and Institute of Materia Medica, Chinese Academy of Medical Sciences.

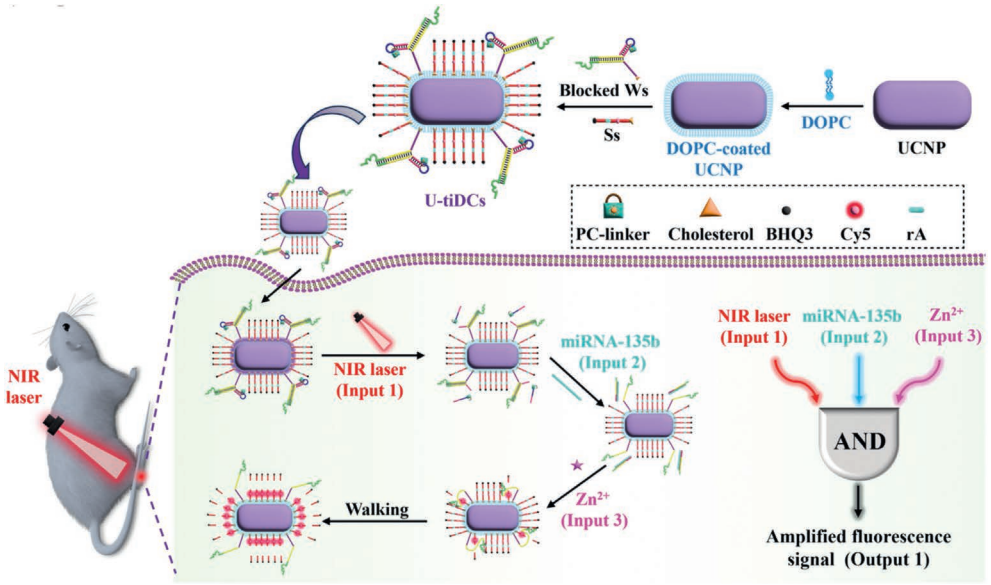


Fig. 1. Scheme showing the construction of U-tiDCs and their application in spatiotemporally precise *in vivo* fluorescence imaging.

output signal *via* programmable strand displacement reactions governed by thermodynamic equilibrium and reaction kinetics [21]. This capability has enabled diverse applications including point-of-care analysis [22], disease diagnosis [23], and biotherapy [24]. Consequently, integrating DCs into fluorescent probes enables multiplexed stimuli inputs to converge into a single fluorescence signal readout. Previous report has demonstrated that the integration of UCNPs as nanocarriers and photocontrol units for DCs can achieve multiplexed *in vivo* molecular imaging with high spatiotemporal resolution [3]. Despite these advances, the inherent complexity of multi-input circuit design and current limitations in scalability pose challenges for practical translation and widespread implementation.

In this study, a double-blocking strategy was novelty proposed to develop UCNPs-assisted tri-input DNA circuits (U-tiDCs), enabling spatiotemporally precise *in vivo* fluorescence imaging (Fig. 1). For proof-of-concept demonstration, a Zn^{2+}-specific DNAzyme-based walker system served as the model platform, with NIR light, miRNA-135b, and Zn^{2+} as orthogonal input stimuli. The U-tiDCs were designed by introducing a photocleavable (PC) linker-contained hairpin-structured strand as the first blocking unit to lock the miRNA-complementary strand, and by using the miRNA-complementary strand as the second blocking unit to spatially inhibit the walker strand. Through modification with cholesterol molecules, the tiDCs can assemble onto the hydrophobic surface of UCNPs. Upon delivery to target tissues, NIR irradiation (Input 1) induced photolysis of the PC linker, disabling the first blocking unit and exposing a toehold domain. Subsequently, miRNA-135b (Input 2) triggered toehold-mediated strand displacement to release the second blocking unit. Upon introduction of Zn^{2+} (Input 3), unlocked DNAzyme walkers catalytically cleave fluorophore-quencher dual modified substrate strands, thereby achieving amplified *in vivo* fluorescence imaging. This modular design not only extends programmable targeting to a broader spectrum of *in vivo* biomarkers but also elevates diagnostic sensitivity and therapeutic precision.

Given the established roles of miRNAs and metal ions in diverse pathological processes [25], miRNA-135b and Zn^{2+} were selected as model targets to validate the operational capability of tiDCs. Our previous work has demonstrated the advantage of fluid DNAzyme-triggered walking systems in accelerating the reaction kinetics and improving amplification efficiency [26]. Therefore, fluid tiDCs were herein constructed *via* cholesterol-mediated co-assembly of blocked walker strands (Ws) and substrate strands (Ss), as depicted in Fig. 2A. The cholesterol-modified Ws was functionally blocked through engineering of a hairpin-structured lock strand (Ls), which sterically occludes the binding arm of the Zn^{2+}-specific 8–17 DNAzyme. This Ls carries an anti-miRNA-135b sequence containing a PC linker. The Ss strand was functionalized with a cholesterol moiety at the 5′ terminus, a Cy5 fluorophore in the middle, and a BHQ3 quencher at the 3′ terminus, respectively. Following incubation, cholesterol-modified blocked Ws and Ss co-assembled into DNA micelles. Upon UV exposure, the PC linker in the blocked Ls undergoes UV light (Input 1)-mediated photolysis, exposing a toehold domain and enabling hybridization with miRNA-135b (Input 2). The higher binding affinity of miRNA-135b initiated toehold-mediated strand displacement, releasing Ls fragment from the micelles. Subsequent Zn^{2+} (Input 3) addition activated the walking system, catalyzing continuous cleavage of Ss. This cleavage spatially separated Cy5 from BHQ3, restoring Cy5 fluorescence for signal output. Thus, the tiDCs generated fluorescent signals exclusively in the presence of all three inputs (UV light, miRNA-135b, and Zn^{2+}), and the corresponding truth table can be summarized in Fig. 2B.

To validate the sequential activation of tiDCs, native polyacrylamide gel electrophoresis (PAGE) analysis was firstly conducted. As shown in Fig. 2C, a single band with consistent electrophoretic mobility in Lanes 1-4 confirmed structural homogeneity of all individual strands (Table S1 in Supporting information for the sequence). In Lane 5, a band exhibiting slower mobility corresponded to the complex formed between the miRNA-135b mimic and the cleavage product of Ls. Following incubation of Ws and Ls, a new band with retarded electrophoretic mobility appeared (Lane 6), indicating successful formation of blocked Ws. Upon UV light irradiation, photocleavage of PC linkers in Ls disrupted the hairpin structure, cleaving them into two distinct DNA fragments (Lane 7). Direct addition of miRNA-135b mimics alone induced no detectable structural changes in blocked Ws (Lane 8), confirming that light-triggered deblocking is prerequisite for miRNA recognition. When both UV light and miRNA-135b were present (Lane 9), bands corresponding to photocleavage products and strand displacement intermediates were observed, confirming that UV light irradiation and

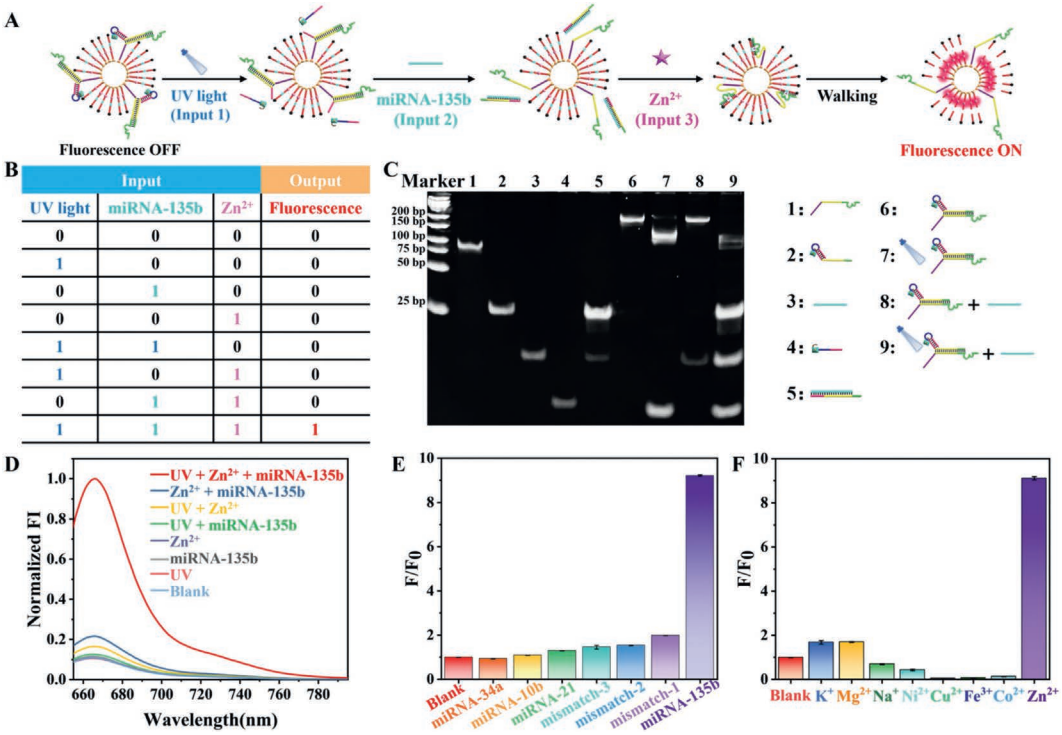


Fig. 2. (A) Scheme showing the response mechanism of fluidic tiDCs, and (B) the corresponding truth table. Input states were defined as "1" for the introduction of UV light, miRNA-135b, or Zn^{2+}, and "0" for their absence. The output state was designated "1" as fluorescence signal generation and "0" for no detectable signal. (C) Native PAGE analysis of the tiDCs formation, and their response toward UV light and miRNA-135b mimic. (D) Fluorescence spectra of tiDCs after different combinations of inputs. Selectivity of tiDCs toward (E) miRNA-135b mimic against different miRNA mimics in the presence of 200 μmol/L Zn^{2+}, and toward (F) Zn^{2+} against other metal ions in the presence of 30 nmol/L miRNA-135b mimics. F_0 and F represent the fluorescence intensity of tiDCs before and after addition of Zn^{2+}. The error bars represent the standard deviation derived from three independent replicates. Data are presented as mean ± standard deviation ($n = 3$).

miRNA-135b hybridization are both required to unblock Ws. Due to the relatively low molecular weights of both Ss and its cleavage products, supplementary PAGE analysis of the DNAzyme-triggered walking system is provided in Fig. S1 (Supporting information). In the absence of Zn^{2+}, both Ws and Ss remained thermodynamically stable. However, upon Zn^{2+} addition, the Ss underwent specific cleavage into smaller fragments, confirming successful operation of the walking system. After PAGE confirmation of sequential activation, the Boolean logic response of tiDCs to all three inputs under optimized conditions (Fig. S2 in Supporting information) was validated. The tiDCs maintained a silent state (Output = 0) for all incomplete input conditions, including single inputs [(1,0,0), (0,1,0), (0,0,1)] and dual inputs [(1,1,0), (1,0,1), (0,1,1)], as evidenced by negligible fluorescence intensity changes (Fig. 2D, and Fig. S3A in Supporting information). Only when all three inputs were present simultaneously (1,1,1), it generated significant fluorescence enhancement, yielding Output = 1. The reaction dynamics further validated this selective activation, with a substantial signal increase occurring exclusively upon the simultaneous introduction of all three inputs (Fig. S3B in Supporting information). As shown in Fig. S4 (Supporting information), the fluorescence response of the tiDCs exhibited dose-dependent modulation by UV irradiation (Fig. S4A), miRNA-135b concentration (Fig. S4B), and Zn^{2+} concentration (Fig. S4C). As shown in the insets of Figs. S4B and C, the linear regression equations were $F/F_0 = 1.446\ \lg[\text{miRNA-135b}] + 7.226$ ($R^2 = 0.995$) and $F/F_0 = 0.0479\ [Zn^{2+}] + 1.30$ ($R^2 = 0.995$), respectively. The system demonstrated high sensitivity, with a limit of detection (LOD) of 10.1 fmol/L for miRNA-135b and 0.179 μmol/L for Zn^{2+}, calculated based on the $3\sigma/k$ rule. Given that physiological miRNA-135b and Zn^{2+} concentrations occur in the nanomolar and micromolar range [27,28], respectively, the achieved LODs readily satisfy the sensitivity requirements for intracellular and *in vivo* imaging applications. High selectivity was maintained for miRNA-135b against analogs (Fig. 2E) and for Zn^{2+} over competing metal ions (Fig. 2F). Collectively, these results confirm robust implementation of the predesigned AND logic operation.

Following validation of tiDCs feasibility, 1,2-dioleoyl-*sn*-glycero-3-phosphocholines (DOPCs)-coated UCNPs acted as bifunctional substrates for *in vivo* delivery and NIR-to-UV transduction, enabling tiDCs assembly through cholesterol-phospholipid interactions (Fig. 1). Transmission electron microscopy (TEM) characterization revealed monodisperse UCNPs were rod-shaped with a length of 56 nm and a width of 32 nm (Fig. 3A). Under 980 nm excitation, these UCNPs exhibited strong upconversion luminescence at 345 and 362 nm (Fig. 3B), precisely matching the PC linker's activation spectrum. This enabled U-tiDCs operation with deep tissue penetration *in vivo*. Subsequent functionalization with tiDCs had negligible impact on nanoparticle morphology or size of UCNPs, evidenced by the appearance of uniform phospholipid membrane encapsulation of UCNPs (Fig. 3C). The characteristic absorbance peaks of DNA (260 nm) [29] and of Cy5/BHQ3 (650 nm) [30], further verified successful construction of U-tiDCs (Fig. 3D). As revealed by zeta potential analysis, the surface zeta potential of UCNPs shifted from +3.85 mV to -3.2 mV following DOPCs coating, and further dropped to -27.2 mV upon addition of tiDCs (Fig. 3E). This sequential potential change firmly confirms the successful formation of U-tiDCs. Crucially, the U-tiDCs remained inactive with single or dual inputs, generating output = 1 only upon simultaneous presence of NIR light, miRNA-135b, and Zn^{2+} (Fig. 3F), confirming NIR-activatable molecular logic operation.

Prior to intracellular imaging studies, the biocompatibility of U-tiDCs and biosafety of 980 nm irradiation were evaluated. As shown in Figs. S5A and B (Supporting information), neither U-tiDCs nor Zn^{2+} significantly reduced viability in rheumatoid

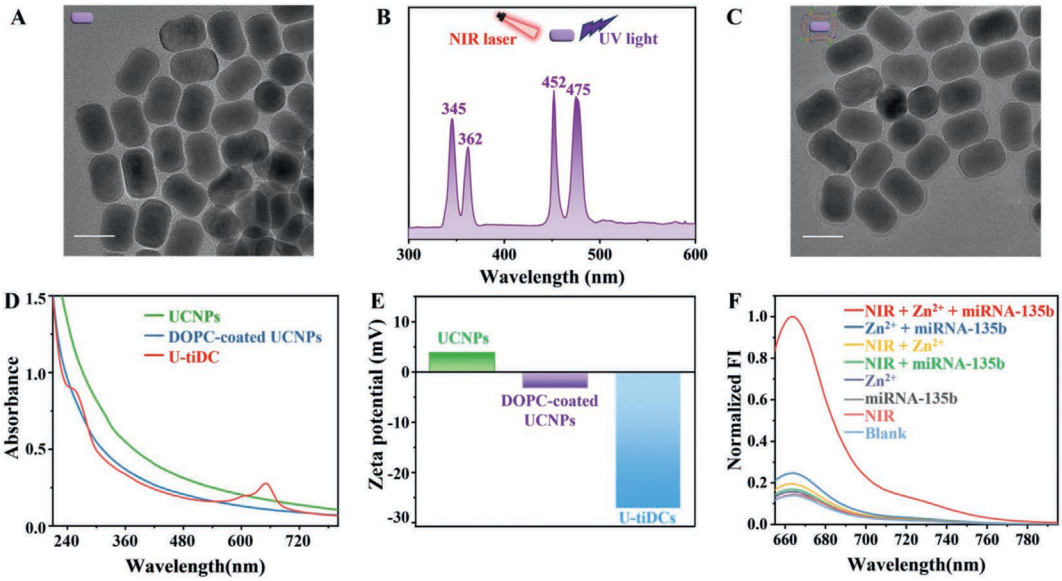


Fig. 3. TEM images of (A) UCNPs and (C) U-tiDCs. Scale bar: 50 nm. (B) Upconversion luminescence spectrum of UCNPs under 980 nm laser irradiation. (D) UV-vis absorption spectra and (E) zeta potential of UCNPs, DOPC-coated UCNPs, and U-tiDCs, respectively. (F) Fluorescence spectra of U-tiDCs after different combinations of inputs.

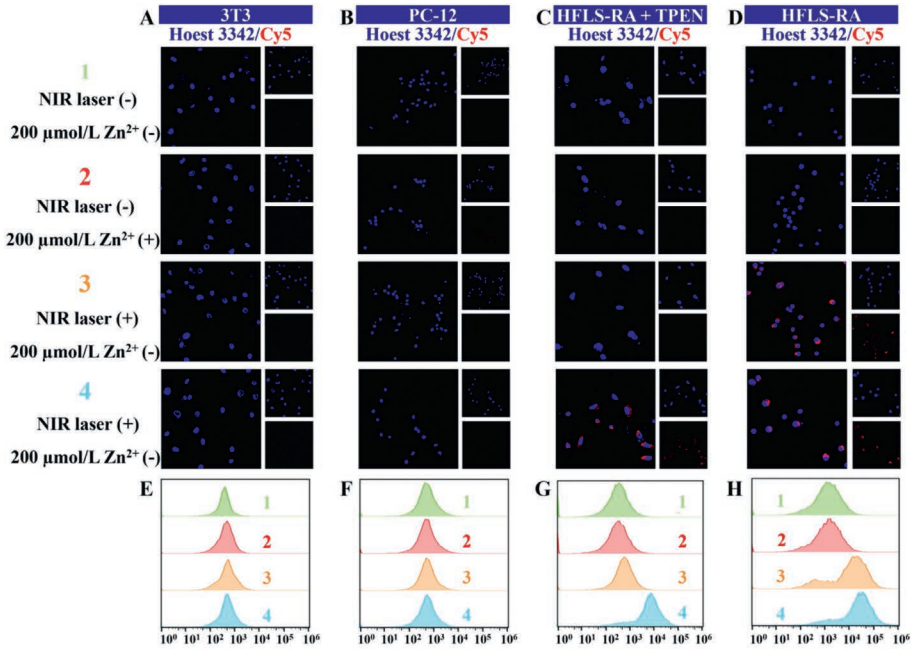


Fig. 4. CLSM images of (A) 3T3 cells, (B) Aβ_{25-35}-pretreated PC-12 cells, (C) TPEN-pretreated HFLS-RA cells, and (D) HFLS-RA cells under different experimental conditions. Flow cytometry analysis of (E) 3T3 cells, (F) Aβ_{25-35}-pretreated PC-12 cells, (G) TPEN-pretreated HFLS-RA cells, and (H) HFLS-RA cells under corresponding conditions.

arthritis fibroblast-like synoviocyte HFLS-RA cells after 24 h exposure. Crucially, NIR irradiation at a power density of 2.5 W/cm^2 for 20 min (2 min break after irradiation for 1.5 min) showed no observable cytotoxic effects, thereby validating the safety of this laser modality for biological applications. To quantify time-dependent cellular uptake kinetics, confocal laser scanning microscopy (CLSM) and flow cytometry analysis were performed on cells after incubating with U-tiDCs (unlabeled with BHQ3) for 0, 0.5, 1.0, 2.0, 3.0, and 4.0 h. Intracellular fluorescence intensity exhibited time-dependent enhancement, plateauing after 3.0 h of incubation (Fig. S5C in Supporting information). Subcellular localization analysis confirmed predominant cytoplasmic distribution of the internalized U-tiDCs. Flow cytometry independently validated these kinetics, establishing 3.0 h as the optimal incubation time for maximal cellular uptake (Fig. S5D in Supporting information).

Subsequently, the intracellular imaging capability of the developed U-tiDCs was evaluated in different cell lines. For the fibroblast cell line (3T3), both miRNA-135b and Zn^{2+} were expressed at low levels [31,32]. In the Aβ_{25-35}-treated pheochromocytoma cell line (PC-12), miRNA-135b was downregulated, whereas Zn^{2+} was present at elevated levels [33,34]. By contrast, both miRNA-135b and Zn^{2+} were highly expressed in the HFLS-RA cells [35,36]. Due to low endogenous miRNA-135b in 3T3 (Figs. 4A and E) and Aβ_{25-35}-treated PC-12 cells (Figs. 4B and F), U-tiDCs-treated cells exhibited negligible Cy5 fluorescence under dual NIR light/Zn^{2+} stimulation, confirming AND-gate inactivity without sufficient miRNA-135b. To further delineate specific role

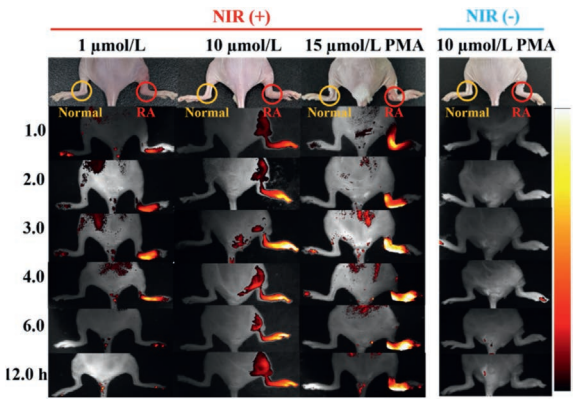


Fig. 5. Time-dependent merged images of RA-bearing mice with or without NIR irradiation.

of Zn^{2+} in U-tiDCs activation, intracellular Zn^{2+} pools of HFLS-RA cells were depleted using high-affinity Zn^{2+} chelators of *N*,*N*,*N*′,*N*′-tetrakis(2-pyridinylmethyl)-1,2-ethanediamine (TPEN). Despite sustained high miRNA-135b expression, TPEN treatment abolished activation signals (Figs. 4C and G). However, intracellular fluorescence was restored upon extracellular addition of 200 μmol/L Zn^{2+}, confirming Zn^{2+} is indispensable for U-tiDCs activation. In U-tiDCs-treated HFLS-RA cells, fluorescence emission was strictly NIR illumination-dependent (Figs. 4D and H), demonstrating NIR-mediated photocontrol for spatiotemporally precise imaging. Collectively, these results experimentally validate that U-tiDCs activation requires simultaneous recognition of all three inputs, ensuring spatiotemporally precise cell imaging with high specificity.

Motivated by the favorable *in vitro* performance, the utility of U-tiDCs in *in vivo* imaging was systematically investigated. All animal experiments were approved by the Animal Ethics Committee of Guangxi Normal University. Given the established co-overexpression of Zn^{2+} and miRNA-135b in arthritic joints [31,32], rheumatoid arthritis (RA)-bearing mouse model was established to assess the U-tiDCs' *in vivo* imaging capability. As shown in Fig. S6 (Supporting information), RA was induced in the right ankle *via* sequential injection of lipopolysaccharide (LPS) and phorbol-12-myristate-13-acetate (PMA) with different concentrations (1, 10, and 15 μmol/L), while the left ankle received normal saline as an internal control. Thirty minutes post-induction, the U-tiDCs were administered to both ankles. After 3 h, both ankles were then subjected to 980 nm laser irradiation (2.5 W/cm^2, 20 min), followed by fluorescence imaging. Visual inspection confirmed classic RA formation in the LPS/PMA-injected right ankle, exhibiting hallmark inflammatory signs including erythema and edema (Fig. 5). This provided a pathologically relevant target region for evaluating U-tiDCs performance in RA pathophysiology. At 1 μmol/L PMA, significant fluorescence signal of Cy5 was observed, indicating that LPS/PMA-induced inflammation enables U-tiDCs activation. Although some background autofluorescence from the tissue was discernible [37,38], higher PMA concentrations (10–15 μmol/L) further enhanced fluorescence intensity in a dose-dependent manner. This indicates elevated PMA levels increase local recruitment/retention of miRNA-135b and Zn^{2+} at inflammation sites, thereby boosting U-tiDCs activation efficiency. Crucially, LPS/PMA-treated inflamed ankles showed no signal without NIR irradiation (rightest column, Fig. 5), and saline-treated control ankles remained dark even in the presence of U-tiDCs administration and NIR irradiation together. This confirms strict three-input AND-gate behavior of U-tiDCs, namely fluorescence occurs only when NIR light and LPS/PMA-induced biomarkers (Zn^{2+}/miRNA-135b) are simultaneously present, enabling spatiotemporally controlled imaging of RA pathology with high specificity.

After demonstrating the feasibility of U-tiDCs in *in vivo* fluorescence imaging, hemolysis assays were performed to evaluate their biocompatibility. As shown in Fig. S7 (Supporting information), U-tiDCs induced minimal hemolysis at concentrations from 25 μg/mL to 500 μg/mL, demonstrating excellent blood compatibility. After conducting *in vivo* fluorescence imaging, RA-bearing mice was sacrificed for *ex vivo* analysis. Fluorescence images of major organs (heart, liver, spleen, lungs, and kidneys) revealed negligible background accumulation in normal organs (Fig. S8A in Supporting information). Hematoxylin and eosin (H&E) staining confirmed no pathological abnormalities in any organs (Fig. S8B in Supporting information), further validating biosafety of U-tiDCs.

In summary, a novel double-blocking strategy to construct U-tiDCs was developed for high-spatiotemporal-precision *in vivo* fluorescence imaging. The tiDCs design implements sequential blocking, namely a miRNA-complementary strand spatially inhibits the DNAzyme walker strand, and a hairpin-structured blocker incorporating a PC linker. Using UCNPs for targeted delivery and NIR-to-UV conversion, the engineered U-tiDCs enabled spatiotemporally precise visualization of arthritis. This proof-of-concept study establishes a programmable framework for designing multi-input DCs, which can be readily adapted through rational sequence design to target diverse biomarker combinations and disease contexts, thereby advancing diagnostic and therapeutic precision.

CRediT authorship contribution statement

Liuyan Zhou: Writing – original draft, Validation, Methodology, Investigation, Formal analysis, Data curation, Conceptualization. **Luyin Wang:** Writing – original draft, Validation, Investigation, Data curation. **Xiaolu Li:** Validation, Investigation. **Meiling Ren:** Validation, Investigation. **Shengqiang Hu:** Writing – review & editing, Writing – original draft, Supervision, Resources, Project administration, Funding acquisition, Data curation, Conceptualization. **Mengjiao Huang:** Methodology, Funding acquisition. **Shulin Zhao:** Supervision, Methodology. **Liangliang Zhang:** Writing – review & editing, Supervision, Project administration, Funding acquisition, Conceptualization.

Declaration of competing interest

The authors declare that they have no known competing financial interests or personal relationships that could have appeared to influence the work reported in this paper.

Acknowledgments

This work was supported by the National Natural Science Foundation of China (Nos. 22204025, 22364005, 22466008), Specific Research Project of Guangxi for Research Bases and Talents (No. GUIKEAD23026209), BaGui Youth Top Talent Project of Guangxi, Innovation Project of Guangxi Graduate Education (Nos. YCBZ2024103, XJCY2022010), and College Student Innovation and Entrepreneurship Training Program Project (No. 202410602048).

Supplementary materials

Supplementary material associated with this article can be found, in the online version, at doi:10.1016/j.cclet.2025.112234.

References

[1] J. Zhan, Z. Liu, R. Liu, J.J. Zhu, J. Zhang, Anal. Chem. 94 (2022) 16622–16631.
[2] T. Tu, S. Huan, X. Feng, et al., Angew. Chem. Int. Ed. 64 (2025) e202424684.
[3] Y. Mi, J. Zhao, H. Chu, et al., Anal. Chem. 93 (2021) 2500–2509.
[4] Y. Hu, J. Yu, M. Xu, K. Pu, J. Am. Chem. Soc. 146 (2024) 12656–12663.
[5] Y. Zheng, X. Ma, S. Zhou, et al., Anal. Chem. 97 (2025) 8370–8377.

[6] Y.X. Zhang, Q. Yang, L.N. Zhu, et al., Anal. Chem. 96 (2024) 7747–7755.
[7] Y.W. Li, H.C. Zhang, G. Guo, G.F. Hu, L. Wang, Anal. Chem. 92 (2020) 11739–11746.
[8] J. Zhao, H.Q. Chu, Y. Zhao, Y. Lu, L.L. Li, J. Am. Chem. Soc. 141 (2019) 7056–7062.
[9] L. Li, X.T. He, Y. Zhang, et al., Anal. Chem. 97 (2025) 768–774.
[10] P. Liu, S.L. Zhang, T.T. Zhang, et al., Chin. Chem. Lett. 37 (2026) 110966.
[11] X.K. Chen, X.D. Zhang, L. Liu, Y. Chen, Y.L. Zhao, J. Am. Chem. Soc. 146 (2024) 34475–34490.
[12] S.Q. Hu, L.X. Huang, L.Y. Zhou, et al., Anal. Chem. 95 (2023) 3830–3839.
[13] L.F. Pang, X.L. Tang, L.J. Yao, L.Y. Zhou, et al., Chem. Sci. 14 (2023) 3070–3075.
[14] L.N. Xu, M. Xu, X. Sun, et al., ACS Nano 17 (2023) 2039–2052.
[15] M.B Cooley, D. Wegierak, R. Perera, et al., ACS Nano 18 (2024) 33181–33196.
[16] H.Q. Chu, J. Zhao, Y.S. Mi, Y.L. Zhao, L.L. Li, Angew. Chem. Int. Ed. 58 (2019) 14877–14881.
[17] J. Zhang, P. Zhao, W. Li, et al., Angew. Chem. Int. Ed. 61 (2022) e202117562.
[18] N.N. Lin, Y. Ouyang, Y.L. Qin, et al., J. Am. Chem. Soc. 146 (2024) 20685–20699.
[19] M.Y. Ye, S.Q. Hu, L.Y. Zhou, et al., Anal. Chem. 94 (2022) 17645–17652.
[20] K. Morihiro, N. Ankenbruck, B. Lukasak, A. Deiters, J. Am. Chem. Soc. 139 (2017) 13909–13915.
[21] X.W. Xiong, M.S. Xiao, W. Lai, et al., Angew. Chem. Int. Ed. 60 (2021) 3397–3401.
[22] Y. Gao, X. Fan, X.C. Zhang, et al., Anal. Chem. 97 (2025) 2402–2410.
[23] X.Z. Meng, X.Y. Zhou, W.J. Yan, D.D. Chen, S. Bi, Nano Lett. 25 (2025) 10354–10361.
[24] A. Ishaqat, X.F. Zhang, Q. Liu, L.F. Zheng, A. Herrmann, J. Am. Chem. Soc. 145 (2023) 12465–12474.
[25] J.Y. Zhan, Z. Liu, R. Liu, J.J. Zhu, J.J. Zhang, Anal. Chem. 94 (2022) 16622–16631.
[26] L.Y. Zhou, X.K. Li, L.Y. Wang, et al., Anal. Chem. 95 (2023) 18497–18503.
[27] S. Kadkhoda, S. Eslami, B. Mahmud Hussen, S. Ghafouri-Fard, Front. Genet. 13 (2022) 973585.
[28] J. Gumulec, M. Masarik, S. Krizkova, et al., Curr. Med. Chem. 18 (2011) 5041–5051.
[29] S. Lee, S. Pandit, G. Gilman, A. Bhattacharya, D. Samanta, Anal. Chem. 97 (2025) 12267–12275.
[30] X. Jin, Y.Z. Liu, O. Alkhamis, et al., Anal. Chem. 94 (2022) 10082–10090.
[31] J. Lim, J.S. Hwang, S. Beom Seo, et al., Chem. Eng. J. 448 (2022) 137637.
[32] B.N. Chen, P.Y. Yu, W.N. Chan, et al., Signal Transduct. Target. Ther. 9 (2024) 6.
[33] P.J. Ghumatkar, S.P. Patil, V. Peshattiwar, et al., N-S Arch. Pharmacol. 392 (2019) 327–339.
[34] H. Kozlowski, M. Luczkowski, M. Remelli, D. Valensin, Coord. Chem. Rev. 256 (2012) 2129–2141.
[35] S.J. Chen, Z.H. Luo, X.G. Chen, Cell Cycle 20 (2021) 1107–1121.
[36] B. Kim, H.Y. Kim, B.R. Yoon, et al., Sci. Signal. 15 (2022) eabi7400.
[37] G.S. Hong, A.L. Antaris, H.J. Dai, Nat. Biomed. Eng. 1 (2017) 0010.
[38] S. Diao, G.S. Hong, A.L. Antaris, et al., Nano Res. 11 (2018) 1069–1081.